

Assessment of high-intensity focused ultrasound treatment of rodent mammary tumors using ultrasound backscatter coefficients

Jeremy P. Kemmerer, Goutam Ghoshal, Chandra Karunakaran, and Michael L. Oelze

Bioacoustics Research Laboratory, Department of Electrical and Computer Engineering, University of Illinois at Urbana-Champaign, 405 North Mathews, Urbana, Illinois 61801

(Received 28 September 2012; revised 17 January 2013; accepted 21 February 2013)

Fischer 344 rats with subcutaneous mammary adenocarcinoma tumors were exposed to therapeutic ultrasound at one of three exposure levels (335, 360, and 502 W/cm² spatial-peak temporal-average intensity). Quantitative ultrasound estimates were generated from ultrasound radio frequency (RF) data from tumors before and after high-intensity focused ultrasound treatment. Treatment outcome was independently assessed by triphenyl tetrazolium chloride (TTC) staining, histological analysis by a pathologist, and thermocouple data. The average backscatter coefficient (BSC) and integrated backscatter coefficient (IBSC) were estimated before and after therapeutic ultrasound exposure for each tumor from RF data collected using clinical (Ultrasonix Sonix RP) and small-animal (Visualsonics Vevo 2100) array systems. Changes in the BSC with treatment were comparable to inter-sample variation of untreated tumors, but statistically significant differences in the change in the IBSCs were observed when comparing the exposures collectively ($p < 0.10$ for Sonix RP, $p < 0.05$ for Vevo 2100). Several exposure levels produced statistically significant differences in the change in IBSC when examined pair-wise, including two exposures having similar intensities ($p < 0.05$, Vevo 2100). A comparison of the IBSC results with temperature data, histology, and TTC staining revealed that the BSC was not always sensitive to thermal insult and that peak exposure pressure appeared to correlate with observed BSC increases.

© 2013 Acoustical Society of America. [http://dx.doi.org/10.1121/1.4812877]

PACS number(s): 43.80.Sh, 43.80.Cs [DLM]

Pages: 1559–1568

I. INTRODUCTION

A non-invasive and targeted tumor therapy which minimizes damage to healthy tissues would provide a significant resource to clinicians for cancer treatment, as well as greatly improve the quality of life of cancer patients undergoing treatment. High-intensity focused ultrasound (HIFU) can potentially fulfill these surgical criteria and address some of the shortcomings of current cancer treatment options such as chemotherapy or radiation. HIFU therapy is currently approved for clinical use in the United States for treating uterine fibroids, and is undergoing trials for prostate cancer treatment.^{1,2} In addition, clinical trials have been conducted in Europe for HIFU treatment of breast cancer,³ liver cancer,⁴ and benign prostatic hyperplasia.⁵

The efficacy of treating tumors with HIFU has been investigated *in vivo* using animal models. In a number of studies, liver tumors in rodents have been treated using focused ultrasound with outcomes ranging from blood vessel disruption⁶ at low intensity to increasing the mean survival rate⁷ and complete tumor destruction⁸ at even higher intensities. Likewise, in one study of HIFU treatment of a rabbit liver tumor (VX2), no regrowth was observed for tumors treated with two HIFU exposures.⁹

Studies spanning several decades elucidate lesion thresholds of HIFU exposure for different types of tissues.^{10–12} Furthermore, theoretical models for lesion development in tissues have been developed.^{13,14} The process of lesion formation depends on tissue-specific properties such as absorption and perfusion, as well as exposure parameters, such as

exposure time, ultrasound intensity, and transducer beam geometry. Though the mechanism(s) of lesion formation is considered to be principally thermal in nature for low to moderate peak intensities and moderate to high duty cycles,^{15,16} acoustic cavitation produced by HIFU exposure can lead to enhanced energy deposition, deviation of lesion location and shape properties from the transducer geometric focus, and a reduction in control of the therapy application.^{17–19} In addition, acoustic cavitation was found to correlate with the appearance of hyperechoic regions in ultrasound B-mode images *in vivo*.²⁰ The presence of cavitation, if controlled, could enhance the heating effect and lower the HIFU intensity required to produce a therapeutic effect. However, uncontrolled cavitation could negatively impact lesion formation, making it difficult to accurately treat specific tissue margins.

The lesion formation process for HIFU therapy depends on patient-specific tissue properties which may not be possible to accurately estimate non-invasively. Therefore, HIFU treatment feedback in the form of real-time monitoring and assessment is critical for effective therapy. Recent advances in magnetic resonance imaging (MRI) temperature monitoring have made it possible to precisely target and monitor HIFU therapy.^{21,22} However, MRI is expensive, incompatible with many HIFU systems, and has poor temporal resolution with respect to rapid HIFU ablation. Ultrasound imaging suffers from none of these specific drawbacks, and has been actively investigated as a means to non-invasively monitor tissue temperature.^{23,24} Ultrasound elastography has been investigated as a tool to assess the spatial distribution of

lesions in tissues.^{25,26} Also, a substantial, localized increase in ultrasound B-mode image brightening has been observed during HIFU exposures, and has been used to visualize HIFU treatment.²⁷ Still, none of the ultrasound-based techniques have been accepted clinically for monitoring and assessment of HIFU therapy. As an alternative, HIFU experiments in tumor-bearing rats were conducted to determine the suitability of quantitative ultrasound (QUS) for acute assessment of therapy. Specifically, QUS techniques based on backscatter coefficients (BSCs) versus frequency were investigated to assess HIFU treatment.

A growing body of evidence suggests that QUS is sensitive to tissue microstructure, and therefore may be used to discriminate between different types of tumors,²⁸ healthy and diseased tissues,^{29,30} and tissues that have responded to treatment.^{31,32} QUS has been investigated as treatment feedback for chemotherapy and radiation,^{33,34} and sensitivity to cellular-level changes during apoptosis has been observed. QUS has also been investigated for assessment of tumors treated with hyperthermia.³⁵ The aim of this study is to determine the feasibility of using QUS to acutely assess HIFU treatment in subcutaneous rodent tumors *in vivo* and to establish if ultrasound backscatter is sensitive to cellular-level changes induced by coagulative necrosis.

II. MATERIALS AND METHODS

A. Tumor preparation and handling

The experimental protocol was approved by the Institutional Animal Care and Use Committee of the University of Illinois at Urbana-Champaign and satisfied all university and National Institutes of Health rules for the humane use of laboratory animals.

Fischer 344 rats were injected subcutaneously with 500 mammary adenocarcinoma (MAT) cells from a 100 μ l fluid medium once on each side of the abdomen. Tumors were allowed to grow at the injection sites over a 2 to 3 week period, until one tumor was at least 7 mm in diameter. On the day of the treatment, the animal was placed in a custom holder with an affixed anesthesia mask and was anesthetized with isoflurane gas (Fig. 1). The abdomen of each animal was shaved and a dipilatory cream was applied around the site of each tumor. Coupling gel was applied to each tumor, tumor dimensions were measured ultrasonically, and pre-exposure ultrasound assessment scans were recorded. A hypodermic needle thermocouple (HYP-1, Omega, Stamford, CT) was inserted into the skin and directly behind the tumor. The thermocouple location was verified using an ultrasound array probe (MS-200 or MS-250, Visualsonics, Toronto, ON, Canada), and the thermocouple probe cable was taped to the holder to avoid any movement of the thermocouple during exposures. The animal was next placed in a tank of degassed water held at 37 °C. While in the tank, the isoflurane rate was increased to alleviate any pain from HIFU exposure, as well as to slow the breathing of the animal. Pre-exposure assessment scans were taken, and HIFU treatment was conducted. Post-exposure assessment scans were conducted after HIFU exposure, and animals were euthanized immediately afterwards. After euthanasia, each animal

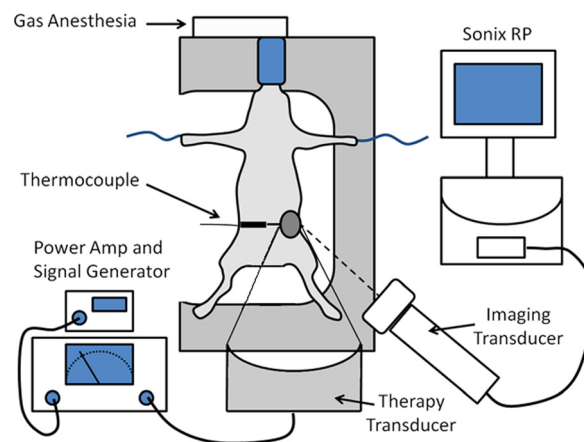


FIG. 1. (Color online) HIFU treatment experimental setup. Tumor targeting was achieved using co-aligned imaging and therapy transducers.

was photographed to determine the location of any effects to the skin. The tumor was removed and its size measured using calipers. The tumor was then bisected, and half of the tumor was placed in triphenyl tetrazolium chloride (TTC) stain for 15 min to assess tumor viability. Both tumor halves were photographed and then placed in formalin for fixation for at least 24 h prior to histological slide preparation.

B. Therapeutic ultrasound

A single-element air-backed focused transducer (1 MHz f/1.1) and an ultrasound image array probe (L14-5/38, Ultrasonix, Richmond, BC, Canada) were placed in an assembly such that the focal region of the HIFU transducer intersected with the imaging plane of the array at a known location on the B-mode image display. The transducer assembly and the animal in its holder were placed in a bath of degassed water held at 37 °C. The tumor was positioned with respect to the assembly using the B-mode image display, and fine adjustments to position were achieved using a positioning system (Daedal, Inc., Harrisburg, PA) controlled by a PC running custom (LabView, National Instruments, Austin, TX) software. In this way, the location of the HIFU transducer focus with respect to the tumor was verified prior to each exposure using the known location of the focus on the B-mode display. Each tumor was exposed to one of three HIFU exposure intensities for 60 s (Table I) at three to five sites. Exposure levels 1 and 2 were chosen to attain a comparable I_{SPTA} with relatively higher peak pressure and duty cycle, respectively, while exposure level 3 was chosen to generate the highest I_{SPTA} . Exposures were placed 2 to 3 mm apart, and selected to cover the tumor surface perpendicular to the beam axis. Because the size, shape, and orientation of the tumors varied, three to five

TABLE I. HIFU treatment exposure levels.

	Exposure 1	Exposure 2	Exposure 3
Peak pressure (MPa)	4.4	3.7	4.4
Duty (%)	50	75	75
Pulse length (ms)	16	48	48
I_{SPTA} (W/cm ²)	335	360	502

sites were required to cover the surface of the tumor while avoiding overlap with previous exposures. The HIFU transducer was connected to a power amplifier (A150 55 dB, ENI, Rochester, NY) and excited by an arbitrary waveform generator (HP 33120a, Agilent Technologies, Santa Clara, CA). During the HIFU exposure, both thermocouple and ultrasound monitoring data were collected continuously. The HIFU system was calibrated in degassed water using a needle hydrophone (HPM075, Precision Acoustics, Dorchester, UK). Calibration intensities for each exposure level are found in Table I. Control animals (sham exposures) were handled and scanned as described, but therapeutic ultrasound exposures did not occur for these animals.

C. Quantitative ultrasound

Prior to placing the animal in the exposure bath, ultrasound image slices were captured with the Vevo 2100 (MS-200 or MS-250 probe) in order to cover the volume of the tumor. Care was taken to avoid air pockets in the coupling gel between the transducer and tumor. Afterwards, the animal was placed in the 37°C bath, and a series of pre-treatment assessment scan slices were collected over the tumor volume with the Sonix RP (L14-5/38). After the HIFU exposures were completed, the tumor volume was again scanned with the Sonix RP. The animal was removed from the tank and finally scanned with the Vevo 2100 after removing the thermocouple. The Sonix RP permitted direct acquisition of the post-beamformed radio frequency (RF) data, while the Vevo 2100 provided in-phase and quadrature data from which the RF data was reconstructed.

Average QUS parameters were estimated for each tumor before and after exposure from a series of rectangular data blocks located inside the tumor region. The data blocks were formed by applying a rectangular window in the axial direction to a series of adjacent scan lines. The average BSC and average integrated backscatter coefficient (IBSC) were estimated for each tumor, both before and after treatment. The BSC was estimated using a reference phantom approach.³⁶ Briefly, a reference phantom of uniform and known scattering and attenuation properties was scanned with the same gain settings and focal depths as were used for the tumor scans. These reference scans were used to compensate for spatially-varying diffraction effects.

The BSC for each data block was estimated from the ratio of power spectra of the sample and the phantom estimated from identical depths

$$\text{BSC}(f) = \frac{PS_{\text{Tumor}}(f)}{PS_{\text{Phantom}}(f)} \times \text{BSC}_{\text{Phantom}}(f). \quad (1)$$

Power spectra for sample and tumor data blocks were estimated by taking the magnitude squared of the fast Fourier transform (FFT) of each windowed RF signal scan line within the corresponding data block and compensating for attenuation. The power spectrum for each data block was then the average of the power spectra computed from individual RF scan lines within the data block. The power spectrum was calculated according to

$$PS_{\text{Tumor}}(f) = \frac{1}{N} \sum_{i=1}^N |\text{FFT}[W_i(t)]|^2 \times \exp[4\alpha L_i], \quad (2)$$

where W_i is a windowed scan line in the data block, FFT denotes the fast Fourier transform, α is the attenuation coefficient, and L_i is the sample depth to the center of each windowed scan line segment. Attenuation for the tumor and the ultrasound gel were estimated to be 0.7 dB/cm/MHz and 0.012 dB/cm/MHz,² respectively, from insertion loss measurements. The square data blocks were 1.5 mm on a side for Vevo 2100 data and 2.5 mm on a side for Sonix RP data. On average, Sonix RP estimates were generated from 5 to 10 data blocks, whereas Vevo 2100 estimates were generated from 50 to 100 data blocks with a 75% overlap.

The IBSC for each tumor was estimated from the area under the average BSC curve as

$$\text{IBSC} = (\Delta f) \times \sum_{m=1}^M \overline{\text{BSC}}(f_m), \quad (3)$$

where f_m is frequency of the m th FFT frequency bin, Δf represents the FFT bin spacing, and $\overline{\text{BSC}}$ is the average of all BSCs within a single tumor. For Sonix RP data, the IBSC was calculated using an analysis bandwidth of 4.5 to 8 MHz, and for Vevo 2100 data, the IBSC was calculated using an analysis bandwidth of 7 to 14 MHz. The change in IBSC with treatment was considered in statistical analysis, and was computed as the post-exposure IBSC less the pre-exposure IBSC. Parametric IBSC images overlaid onto B-mode images appear for Vevo 2100 data and Sonix RP data in Figs. 2 and 3, respectively.

III. EXPERIMENTAL RESULTS

A. Tumor staining

HIFU exposure of the MAT tumors caused visible lesions to form on the skin of the animals where the beam intersected the skin. This was likely caused by the relatively large depth of field of the therapy transducer because the tumor was only 1 to 2 mm from the skin surface. Furthermore, increased pressure at the skin surface was expected because of significant reflection of ultrasound at the interface between skin and water, i.e., the characteristic impedance of the skin surface was greater than the characteristic impedance of the water. However, the HIFU transducer did not touch the skin. These marks provided visual confirmation of correct targeting of the tumor. Upon removal of the tumor, discoloration of the tumor was frequently present, though tumor discoloration was subtle and difficult to detect visually in some cases. For this reason, a section of $n=28$ of the tumors was placed in a stain solution of TTC for 15 min. Photographs of the stained tumor sections were examined and graded based on the amount of stain uptake (Fig. 4). Tumor regions with stain uptake were considered to be viable, whereas regions that did not uptake the stain were non-viable, either due to therapeutic ultrasound treatment or existing tumor necrosis. Tumors with stain uptake in more than 90% of the area of the observed section were scored at level 0. Likewise, tumors showing between 50% and 90% stain uptake were scored at level 1 and with stain uptake in

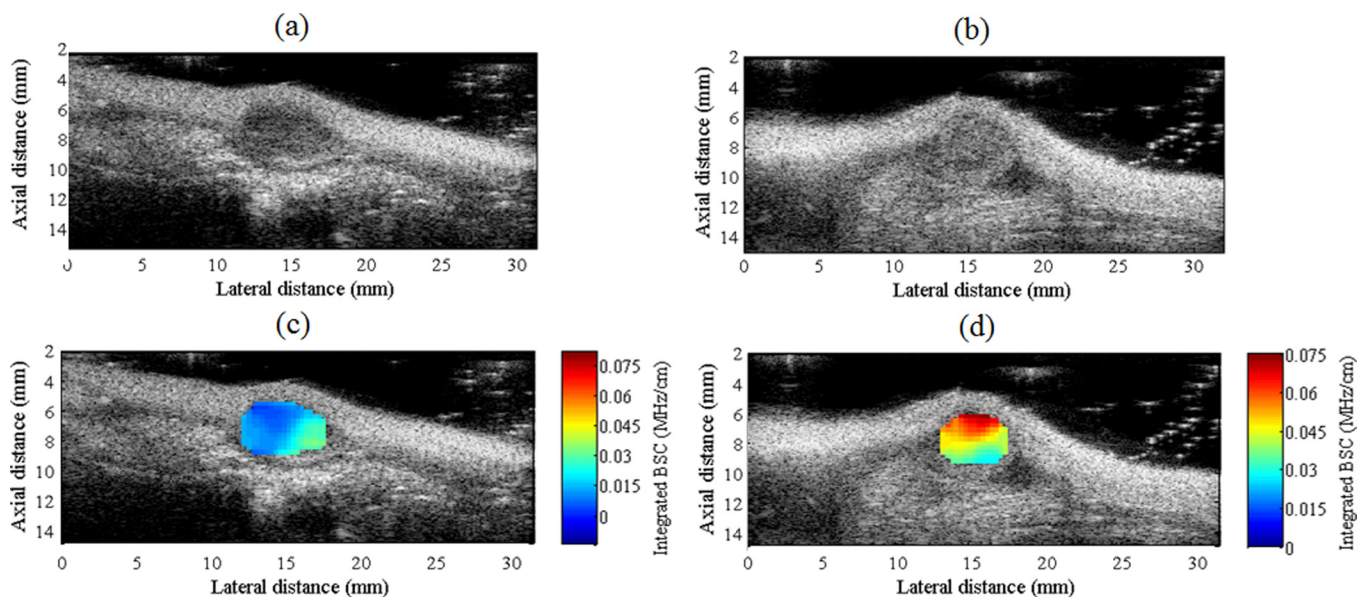


FIG. 2. (Color online) B-modes images [(a),(b)] and parametric IBSC images [(c),(d)] for a MAT tumor pre-treatment [(a),(c)] and post-treatment [(b),(d)], Visualsonics Vevo 2100.

less than 50% of the section were scored at level 2 (i.e., tumors with the largest amount of nonviable tissue).

Uptake scores were lowest and therefore the effect was largest for exposure 3, while TTC scores were comparable for

exposures 1 and 2 (Fig. 4). Boxplots of the change in IBSC as a function of the TTC and histology scoring metrics appear in Fig. 5. Pre-existing tumor necrosis was a confounding factor in TTC staining, because necrotic tumor regions were non-viable, and therefore were not expected to take up the stain. While control tumors showed a consistently high uptake of stain (Fig. 4), the degree of tumor necrosis varied significantly overall.

B. Peak temperature

Temperature measurements were recorded during the HIFU exposure for $n = 35$ tumors. These temperature measurements

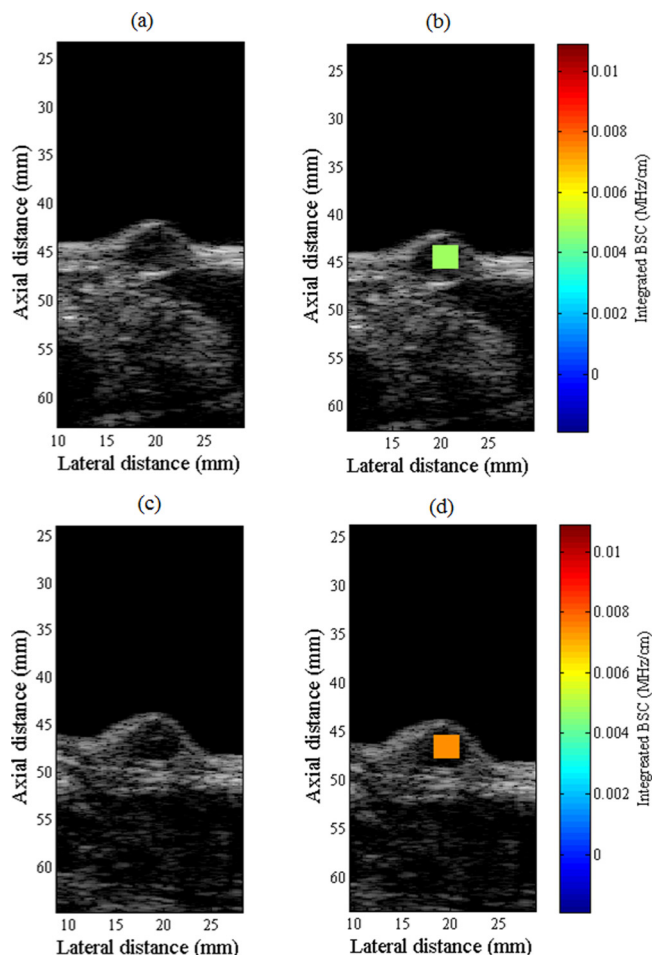


FIG. 3. (Color online) B-modes images [(a),(b)] and parametric IBSC images [(c),(d)] for a MAT tumor pre-treatment [(a),(c)] and post-treatment [(b),(d)], Ultrasonix Sonix RP.

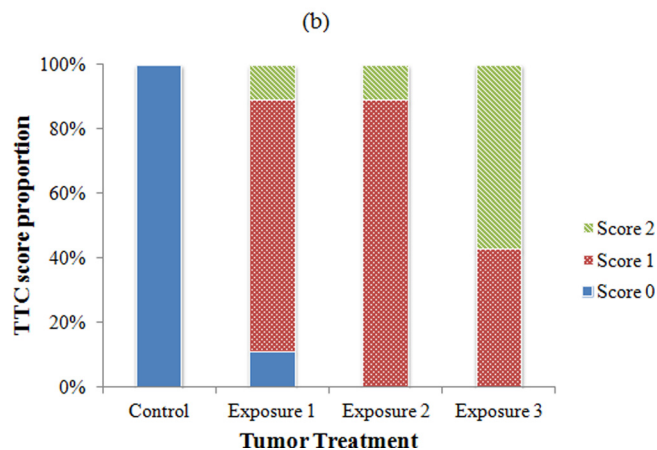
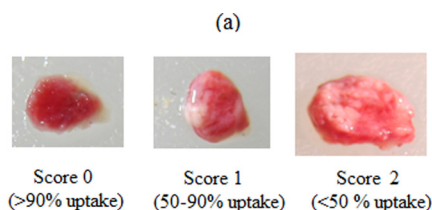


FIG. 4. (Color online) Representative section photograph for each TTC score level (a) and proportion of TTC stain scores for each treatment level (b).

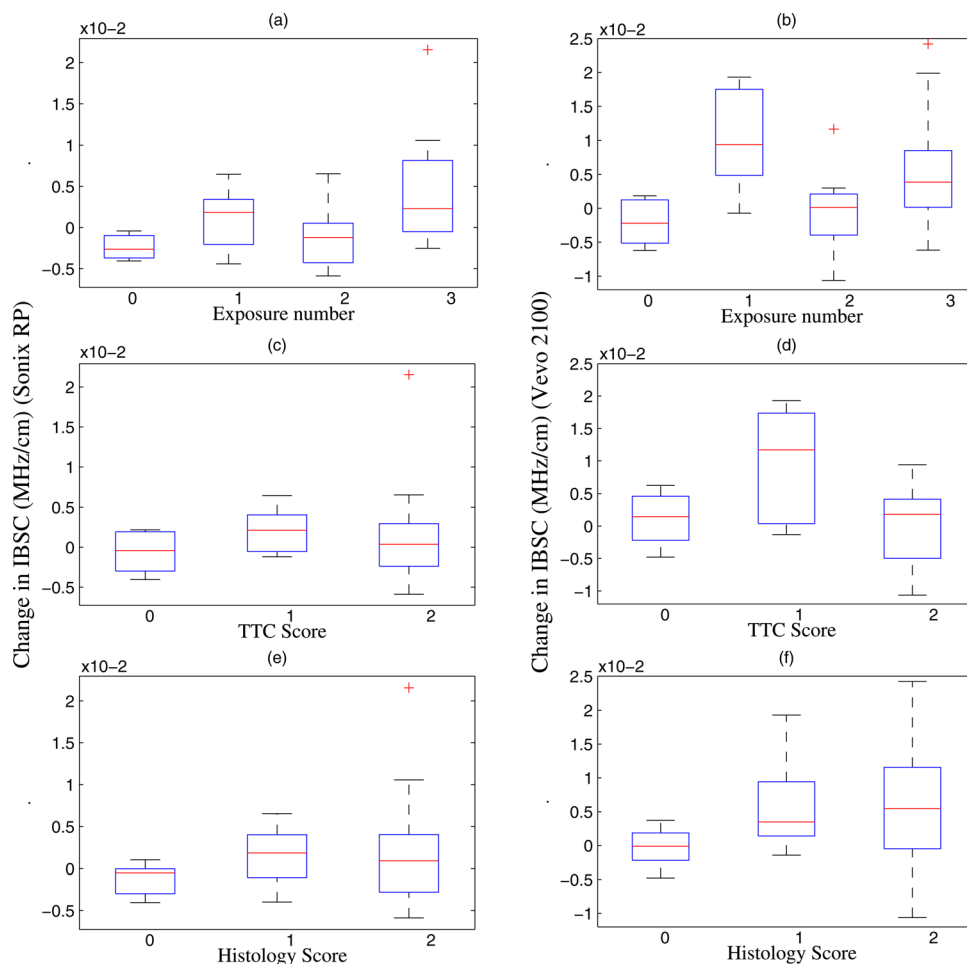


FIG. 5. (Color online) Boxplots (center line is median, whiskers indicate minimum and maximum, + indicates outlier) of the change in IBSC for each exposure [(a),(b)], for each TTC score [(c),(d)], and for each histology score [(e),(f)].

were taken outside of the focal region of the therapy transducer, as the thermocouple was deliberately placed at the edge of the tumor to avoid interaction with the HIFU transducer beam. This placement was guided by the Vevo 2100 system to ensure that the thermocouple was in fact placed on the tumor periphery. The thermocouple probe was not moved between HIFU exposures, and therefore was not positioned at a constant location with respect to the therapy transducer focus. The measured values therefore indicate a lower bound for the peak exposure temperature within the tumor. The average of the peak temperature for each of the exposures was computed for each tumor. This average peak exposure temperature was found to be lowest for exposure 1 (54.4°C), intermediate for exposure 2 (60.4°C), and highest for exposure 3 (63.6°C) (Table II).

C. Quantitative ultrasound

Backscatter coefficients were estimated from $n = 39$ and $n = 33$ tumors for Vevo 2100 and Sonix RP scan data,

TABLE II. Average peak temperature for each exposure level.

Exposure #	Average peak temperature (°C)
1	54.4
2	60.4
3	63.6

respectively (Fig. 6). Three animals were removed from the Vevo 2100 data set because of insufficient tumor size, lack of evidence of correct targeting of the HIFU transducer (no mark on the skin), or death of the animal before post-exposure assessment scans could be conducted. Six additional animals were removed from the Sonix RP data set because of insufficient tumor size or placement of the thermocouple probe such that no data blocks could be selected which did not contain the thermocouple. IBSC estimates were generated for each tumor (Table III).

Analysis of variance (ANOVA) was performed to determine the significance of any differences in the change in IBSC estimates between the four treatment levels (three exposure levels and controls). The change in IBSC with treatment (Fig. 5), as represented by the difference of the pre- and post-exposure IBSC estimates, was selected to normalize the IBSC estimates and to reduce the impact of tumor composition by considering only how much the IBSC changed with treatment. ANOVA revealed a statistically suggestive difference in the change in IBSC between the four treatment levels for Sonix RP data ($p < 0.10$) and a statistically significant difference for the Vevo 2100 data ($p < 0.05$). Upon conducting a Tukey's honest significance difference test to examine pairs of treatment levels, a statistically suggestive difference in the change in IBSC was found

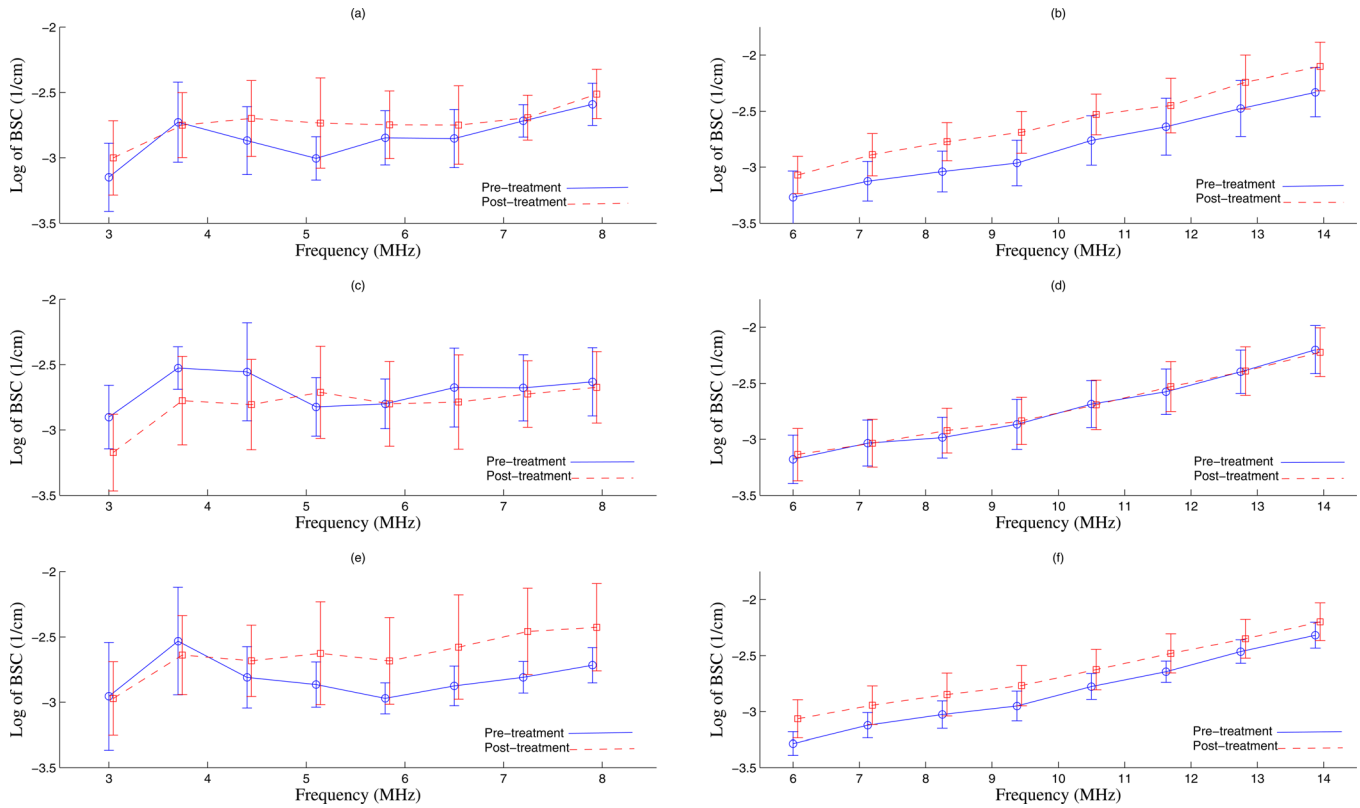


FIG. 6. (Color online) Average BSC estimates for each exposure: Exposure 1 [(a),(b)], exposure 2 [(c),(d)], and exposure 3 [(e),(f)].

between exposure 3 and exposure 2 ($p < 0.10$) for Sonix RP data, and statistically significant differences in IBSC were found between exposure 2 and exposure 1 ($p < 0.05$) and exposure 1 and controls ($p < 0.05$) for Vevo 2100 data. Table IV summarizes these results and includes p -values for ANOVA and all pair-wise comparisons.

D. Histology

Histopathology slides were generated from a cross section of each tumor sample after excision. Tissue sections were stained with hematoxylin and eosin. This two-step process first stained the cell nuclei with hematoxylin, and then stained other structures such as the cellular cytoplasm with eosin. The resulting microscope slides were examined by a pathologist. Major effects identified were dilation and congestion of blood vessels with hemorrhage [Fig. 7(b)] and the presence of thermal artifacts marked by a change in the stain of the cellular cytoplasm [Fig. 7(c)]. Each tumor slide was graded at one of three levels. Level 0 indicated little to no vascular congestion

[Fig. 7(a)]. Level 1 indicated marked peripheral and central vascular congestion and/or acute hemorrhage, but without other tissue thermal artifacts [Fig. 7(b)]. Level 2 indicated the presence of visible tissue thermal damage artifacts, which were identified as a discoloration of the cellular cytoplasm [Fig. 7(c)]. Level 2 was chosen to indicate a higher degree of thermal insult than level 1. Isolated regions of cell cauterization were also identified in some cases, but were not included in the scoring. Figure 8 shows the proportion of each score for each tumor exposure level.

Tumors treated with exposure 3 produced the highest proportion of score 2, indicating that this exposure produced the largest thermal effect based on the pathology scoring used. Two tumors were scored as 0 for this exposure. In this case, the treated regions of the tumors may not have appeared in the examined histology tumor section. Exposures 1 and 2 produced comparable histology scores.

TABLE III. Mean IBSC values before and after HIFU treatment.

Exposure group	Pre-treatment IBSC (RP)	Post-treatment IBSC (RP)	Pre-treatment IBSC (Vevo)	Post-treatment IBSC (Vevo)
Control	0.63 ± 0.2	0.40 ± 0.1	2.44 ± 1.7	2.23 ± 1.7
Exposure 1	0.55 ± 0.2	0.67 ± 0.3	1.43 ± 0.6	2.42 ± 1.0
Exposure 2	0.77 ± 0.4	0.63 ± 0.5	1.79 ± 0.6	1.75 ± 0.8
Exposure 3	0.52 ± 0.2	0.94 ± 0.7	1.46 ± 0.4	2.02 ± 0.9

TABLE IV. Pair-wise comparisons of the change in IBSC (exposures 1 to 3 indicated "1-3", controls by "C"). Statistically suggestive and significant p -values appear in bold.

Exposures compared	p -value (RP)	p -value (Vevo)
1,2,3,C	0.054	0.006
1,C	0.54	0.02
2,C	0.98	0.98
3,C	0.17	0.19
2,1	0.54	0.015
3,1	0.70	0.47
3,2	0.077	0.22

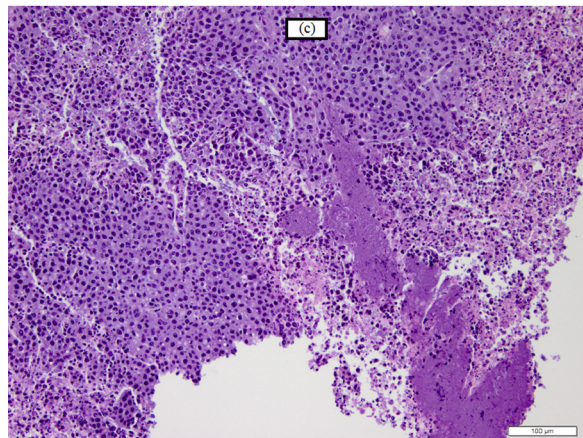
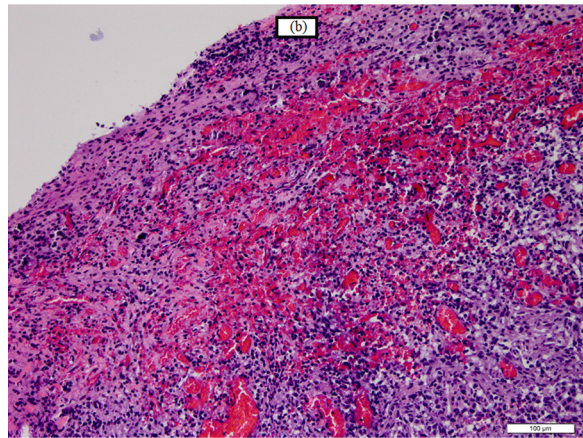
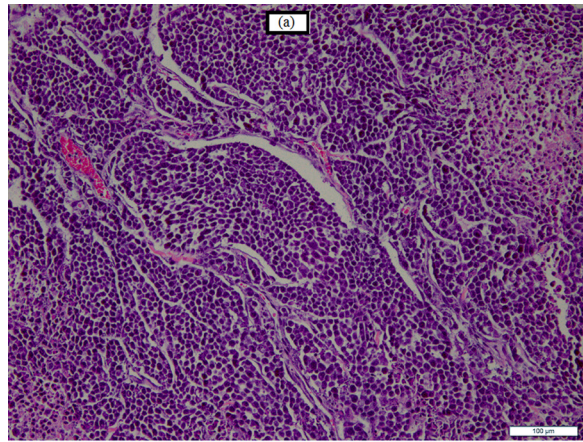


FIG. 7. (Color online) Histology slide image corresponding to a score of 0 (little or no vascular congestion is seen) (a); histology slide image corresponding to a score of 1 (peripheral vascular congestion with hemorrhage) (b); histology slide image corresponding to a score of 2 (thermal effect as determined by cytoplasm discoloration and thermal necrosis) (c). Scale bar is 100 μm .

IV. CONCLUSIONS

QUS techniques were investigated for assessment of HIFU therapy, and HIFU therapy efficacy was independently verified using TTC staining, stained histology sections, and thermocouple data. Thermocouple measurements provided temperature data related to the therapeutic thermal dose. The primary purpose of including the non-ultrasonic effect scores was not to determine the efficacy of HIFU therapy in

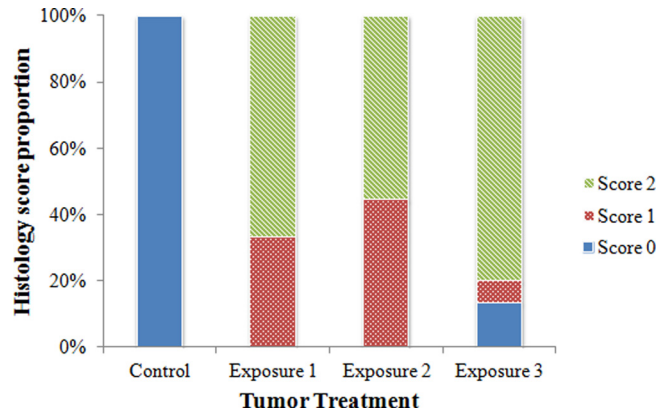


FIG. 8. (Color online) Proportion of histology slide scores for each treatment level as determined by a pathologist.

general, as this to date has been well established, but to rule out ineffective treatment as the cause of a negative QUS detection result. TTC staining and histological scoring indicated that exposure 3, which corresponded to the highest spatial-peak temporal-average intensity, produced the highest scores, and thermocouple temperature measurements demonstrated that exposure 3 produced the largest average temperature increase. Further, treatment effects as quantified by TTC and histology scoring were similar for exposures 1 and 2, while exposure 2 produced peak temperatures that were on average 5 $^{\circ}\text{C}$ higher than exposure 1, though the spatial-peak temporal-average intensities were similar.

Overall, observed changes in BSC estimates with treatment were comparable in magnitude to the variation in BSC estimates between tumor samples. Statistically significant differences between treatment levels were observed for the Sonix RP and Vevo 2100 change in IBSC estimates. However, only Vevo 2100 change in IBSC estimates revealed a statistically significant difference between an exposure group (exposure 1) and the control group. In comparing exposure 1 tumors to controls, which were not exposed to HIFU but otherwise handled and scanned the same way, the significant difference in the change in IBSC suggested that, under these particular exposure conditions, the IBSC was sensitive to HIFU therapy. Comparing exposure 2 to controls revealed that, at a lower peak pressure and higher duty cycle, the IBSC (and therefore the BSC) was relatively insensitive to HIFU treatment. TTC, histology, and thermocouple data do not suggest that a lack of biological effect for exposure 2 would explain this discrepancy.

Comparing results for exposures 1 and 2 revealed important clues regarding the source of the IBSC sensitivity. Exposures 1 and 2 produced a similar I_{SPTA} (335 and 360 W/cm^2 in degassed water, respectively) but achieved this I_{SPTA} in different ways, i.e., through a relatively higher peak pressure or duty cycle, respectively. For the Vevo 2100 data, exposure 1 produced a change in IBSC that was larger than the change in IBSC corresponding to exposure 2, and this difference was statistically significant. In contrast, histology scoring, which was based on the appearance of thermal artifacts, revealed comparable effect scores for exposures 1 and 2 (Fig. 8), and did not suggest that the thermal effects from exposures 1 and 2 were different. Thermocouple data likewise did not suggest

that exposure 1 produced higher temperatures than exposure 2, but in fact demonstrated that exposure 2 temperatures were higher than those for exposure 1. Finally, a comparison of the change in IBSC with TTC and histology did not reveal any apparent correlation between IBSC and effect scores, as would be expected if the detected BSC changes were due to thermal necrosis. From all of these observations, we hypothesize that the statistically significant increase in the change in IBSC observed for exposure 1 Vevo 2100 data was caused by a non-thermal effect related to peak exposure pressure. This hypothesis would explain the increases in IBSC observed for exposures 1 and 3, which produced the highest pressure, and is consistent with *in vivo* studies, which found that non-thermal effects such as cavitation or boiling created hyperechoic regions on B-mode images and were more likely to occur at higher pressure levels.^{19,20} These hyperechoic regions would produce an increase in the BSC and IBSC, consistent with what was observed for exposures 1 and 3.

Exposure 3 produced several treatments with relatively high post-exposure Sonix RP BSC estimates, resulting in a significant difference between exposure 3 and exposure 2 changes in IBSC estimates. This observation may be explained by the relatively higher I_{SPTA} of exposure 3, and again may indicate the presence of a non-thermal mechanism. However, although increases in BSC and IBSC were also observed in the Vevo 2100 data, these increases did not correspond to the same tumors that had increases for the Sonix RP data, and did not produce a significant difference in IBSC between exposure 3 and any other treatment group. This lack of agreement between the two systems may be explained by the time delay of approximately 20 min between Sonix RP and Vevo 2100 assessment scans. While the Sonix RP data was collected within a few minutes of the last HIFU exposure, the Vevo 2100 data was taken after all Sonix RP scans were completed and after transporting the animal to a table for scanning. Thus, any transient phenomena may have been detected differently by these two systems.

The statistically significant increase in IBSC for exposure 1 observed for Vevo 2100 scan data was not observed for the Sonix RP scan data. This result may be explained by the lower interrogation frequency and by the lower spatial resolution of the L14-5/38 imaging probe. Upon comparing the BSC from the Sonix RP with the Vevo 2100 data over their shared bandwidth (6 to 8 MHz), a difference was apparent (Fig. 9). IBSC estimates from 6 to 8 MHz for Sonix RP data were larger than estimates from Vevo 2100 data over this same band to a statistically significant extent ($p < 0.05$). One possible explanation for this difference is the presence of clutter in the Sonix RP data set due to the larger beam width of the L14-5/38 transducer, increasing the potential for strongly scattering objects such as skin to reside within the imaging beam and thereby increase the average BSC estimate. Additionally, no thermocouple was present in the tumor for the Vevo 2100 scans, potentially adding an additional source of clutter for the Sonix RP data. This clutter could have masked treatment effects and lowered the sensitivity of QUS to detecting HIFU treatment. For this reason, the Vevo 2100 scan data were expected to be more sensitive to changes in the BSC.

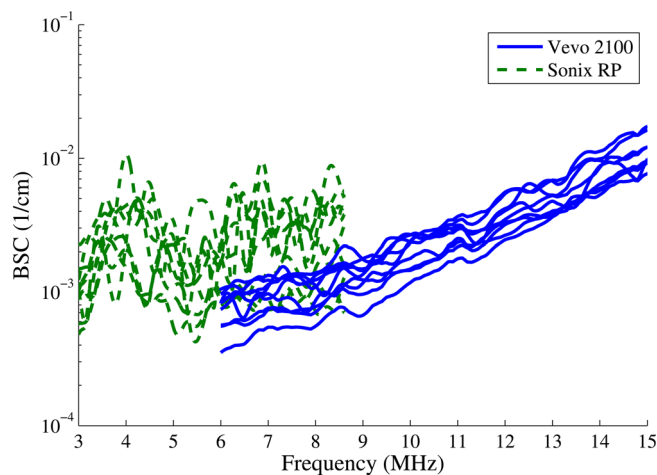


FIG. 9. (Color online) Untreated tumor BSC estimates from L14-5/38 (Sonix RP) and MS-200 (Vevo 2100) transducers.

The results of this study suggest that the BSC was sensitive to a persistent (on the order of an hour) non-thermal effect(s) generated by HIFU treatment, and that peak pressure, rather than I_{SPTA} , was correlated to this sensitivity. The QUS results also highlight the possibility of tumor treatment without any statistically significant change in IBSCs, as illustrated by exposure 2 estimates (Fig. 5, Table IV). We hypothesize that if HIFU therapy is not accompanied by significant non-thermal effects, i.e., as produced by cavitation, that the BSC may be a relatively insensitive parameter for acutely assessing HIFU therapy. This conclusion is also consistent with *ex vivo* findings in liver tissue which concluded that the BSC was relatively insensitive to thermal treatment.³⁷⁻³⁹ In particular, an *ex vivo* rodent liver study revealed that, for a series of water bath treatments, changes to the BSC of rodent liver tissue over frequencies from 8 to 15 MHz were negligible. This hypothesis is also supported by the apparent absence of dramatic morphological changes after HIFU treatment, in contrast to what was reported³³ following other therapeutic modalities which induce apoptosis, rather than coagulative necrosis. We hypothesize that the increases in BSC observed reflect the generation of new scatterers. In this way, lesion detection using the BSC may be complimentary to elastography, since BSC may not be sensitive to thermal coagulation alone, but can be used to detect apparent changes in scattering beneath the treated region due to increased attenuation as well as scattering increases at the site lesion, when they occur.

Future work regarding ultrasonic feedback of HIFU therapy will include improvements based on this study. First, the size and composition of the MAT tumors selected for this study varied substantially. Although care was taken to treat tumors in a range from 7 to 9 mm in the largest dimension, the rapid rate of MAT tumor growth at this target size made close control of tumor size impractical. Larger, more rapidly growing tumors were more likely to exhibit liquefactive necrosis, whereby the tumor tissues were digested and converted to a liquid. The presence of liquefactive necrosis, which is associated with hypoxic cell death,⁴⁰ suggested that these larger tumors had grown too quickly for their blood

supply. The presence of this liquid could modify the absorption of ultrasound energy and impact HIFU treatment. Future studies should place emphasis on selecting a tumor model to produce more uniform tumor sizes and to enable larger tumors to grow without producing significant liquefactive necrosis. Also, some type of passive or active cavitation-monitoring technique should be included during the HIFU exposure to clarify the role of cavitation in generating detectable lesions.

Registration of pre- and post-exposure ultrasound data with histology and TTC staining cross sections will improve future studies. It was observed that the subcutaneous MAT tumors tended to protrude after treatment compared to their orientation before treatment, which made selecting the same tissue region in pre- and post-exposure data sets more subjective. For this reason, only the average BSC for each tumor was used to quantify treatment effects. Registration of ultrasound data with independently determined treatment effects from histology would provide a finer picture of the sensitivity of the BSC to HIFU treatment, as well as offer more specific clues linking BSC changes with tissue morphological features.

ACKNOWLEDGMENTS

The authors would like to acknowledge Rita Miller, D.M.V., Rami Abu-Habsah, and Xin Li for experiment technical assistance, Emily Hartman, R.D.M.S., for assistance with ultrasound scans, Sandhya Sarwate, M.D., for histology slide examination, and Dr. Douglas Simpson for statistical consultation. This work was funded by Grant No. NIH R01-EB008992.

¹E. A. Stewart, W. M. W. Gedroyc, C. M. C. Tempny, B. J. Quade, Y. Inbar, T. Ehrenstein, A. Shushan, J. T. Hindley, R. D. Golden, M. David, M. Sklair, and J. Rabinovici, "Focused ultrasound treatment of uterine fibroid tumors: Safety and feasibility of a noninvasive thermoablative technique," *Am. J. Obstet. Gynecol.* **189**, 48–54 (2003).
²G. K. Hesley, K. R. Gorny, T. L. Henrichsen, D. A. Woodrum, and D. L. Brown, "A clinical review of focused ultrasound ablation with magnetic resonance guidance: An option for treating uterine fibroids," *Ultrasound Quarterly* **24**, 131–139 (2008).
³F. Wu, Z. Wang, Y. Cao, W. Chen, J. Bai, J. Zou, and H. Zhu, "A randomized clinical trial of high-intensity focused ultrasound ablation for the treatment of patients with localized breast cancer," *Br. J. Cancer* **89**, 2227–2233 (2003).
⁴J. E. Kennedy, F. Wu, G. R. ter Haar, F. V. Glesson, R. R. Phillips, M. R. Middleton, and D. Cranston, "High-intensity focused ultrasound for the treatment of liver tumors," *Ultrasonics* **42**, 931–935 (2004).
⁵G. T. Clement, "Perspectives in clinical uses of high-intensity focused ultrasound," *Ultrasonics* **42**, 1087–1093 (2004).
⁶A. K. W. Wood, R. M. Bunte, S. M. Schultz, and C. M. Sehgal, "Acute increases in murine tumor echogenicity after antivascular ultrasound therapy: A pilot preclinical study," *J. Ultrasound Med.* **28**, 795–800 (2009).
⁷F. J. Fry and L. K. Johnson, "Tumor irradiation with intense ultrasound," *Ultrasound Med. Biol.* **4**, 337–341 (1978).
⁸L. Chen, G. ter Haar, C. R. Hill, S. A. Eccles, and G. Box, "Treatment of implanted liver tumors with focused ultrasound," *Ultrasound Med. Biol.* **9**, 1475–1488 (1988).
⁹F. Prat, M. Centarti, A. Sibille, F. A. El Fadil, L. Henry, J. Chapelon, and D. Cathignol, "Extracorporeal high-intensity focused ultrasound for VX2 liver tumors in the rabbit," *Hepatology* **21**, 832–836 (1995).
¹⁰R. M. Lerner and E. L. Carstensen, "Frequency dependence of thresholds for ultrasound production of thermal lesions in tissue," *J. Acoust. Soc. Am.* **54**, 504–506 (1973).
¹¹F. Dunn, J. E. Lohnes, and F. J. Fry, "Frequency dependence of threshold ultrasonic dosages for irreversible structural changes in mammalian brain," *J. Acoust. Soc. Am.* **58**, 512–514 (1975).

¹²L. A. Frizzell, C. A. Linke, E. L. Carstensen, and C. W. Fridd, "Thresholds for focal ultrasonic lesions in rabbit kidney, liver, and testicle," *IEEE Trans. Biomed. Eng.* **4**, 393–396 (1977).
¹³T. C. Robinson and P. P. Lele, "An analysis of lesion development in the brain and in plastics by high-intensity focused ultrasound at low-megahertz frequencies," *J. Acoust. Soc. Am.* **51**, 1333–1351 (1972).
¹⁴C. R. Hill, I. Rivens, M. G. Vaughan, and G. R. ter Haar, "Lesion development in focused ultrasound surgery: A general model," *Ultrasound Med. Biol.* **20**, 259–269 (1994).
¹⁵F. J. Fry, G. Kossoff, R. C. Eggleton, and F. Dunn, "Threshold ultrasonic dosages for structural changes in the mammalian brain," *J. Acoust. Soc. Am.* **48**, 1413–1417 (1970).
¹⁶E. L. Carstensen, M. W. Miller, and C. A. Linke, "Biological effects of ultrasound," *J. Biol. Phys.* **2**, 173–192 (1974).
¹⁷C. C. Coussios, C. H. Farney, G. ter Haar, and R. A. Roy, "Role of acoustic cavitation in the delivery and monitoring of cancer treatment by high-intensity focused ultrasound (HIFU)," *Int. J. Hyperthermia* **23**, 105–120 (2007).
¹⁸M. R. Bailey, V. A. Khokhlova, O. A. Sapozhnikov, S. G. Kargl, and L. A. Crum, "Physical mechanisms of the therapeutic effect of ultrasound (a review)," *Acoust. Phys.* **4**, 369–388 (2003).
¹⁹K. Hynynen, "The threshold for thermally significant cavitation in dog's thigh muscle in vivo," *Ultrasound Med. Biol.* **17**, 157–159 (1991).
²⁰B. A. Rabkin, V. Zderic, and S. Vaezy, "Hyperecho in ultrasound images of HIFU therapy: Involvement of cavitation," *Ultrasound Med. Biol.* **31**, 947–956 (2005).
²¹I. Rivens, A. Shaw, J. Civale, and H. Morris, "Treatment monitoring and thermometry for therapeutic focused ultrasound," *Int. J. Hyperthermia* **23**, 121–139 (2007).
²²C. M. C. Tempny, E. A. Stewart, N. McDannold, B. J. Quade, F. A. Jolesz, and K. Hynynen, "MR imaging-guided focused ultrasound surgery of uterine leiomyomas: A feasibility study," *Radiology* **226**, 897–905 (2003).
²³C. Simon, P. VanBaren, and E. S. Ebbini, "Two-dimensional temperature estimation using diagnostic ultrasound," *IEEE Trans. Ultra. Ferroelect. Freq. Control* **45**, 1088–1098 (1998).
²⁴G. Ghoshal, A. C. Luchies, J. P. Blue, and M. L. Oelze, "Temperature dependent ultrasonic characterization of biological media," *J. Acoust. Soc. Am.* **130**, 2203–2211 (2011).
²⁵R. Righetti, F. Kallel, R. J. Stafford, R. E. Price, T. A. Krouskop, J. D. Hazle, and J. Ophir, "Elastographic characterization of HIFU-induced lesions in canine livers," *Ultrasound Med. Biol.* **25**, 1099–1113 (1999).
²⁶L. Curiel, R. Souchon, O. Roiviere, A. Gelet, and J. Y. Chapelon, "Elastography for the follow-up of high-intensity focused ultrasound prostate cancer treatment: Initial comparison with MRI," *Ultrasound Med. Biol.* **31**, 1461–1468 (2005).
²⁷S. Vaezy, X. Shi, R. W. Martin, E. Chi, P. I. Nelson, M. R. Bailey, and L. A. Crum, "Real-time visualization of high-intensity focused ultrasound treatment using ultrasound imaging," *Ultrasound Med. Biol.* **27**, 33–42 (2001).
²⁸M. L. Oelze and J. F. Zachary, "Examination of cancer in mouse models using high-frequency quantitative ultrasound," *Ultrasound Med. Biol.* **32**, 1639–1648 (2006).
²⁹G. Ghoshal, R. J. Lavarello, J. P. Kemmerer, R. J. Miller, and M. L. Oelze, "Ex vivo study of quantitative ultrasound parameters in fatty rabbit livers," *Ultrasound Med. Biol.* **38**, 2238–2248 (2012).
³⁰J. Mamou, A. Coron, M. Hata, J. Machi, E. Yanagihara, P. Laugier, and E. J. Feleppa, "Three-dimensional high-frequency characterization of cancer lymph nodes," *Ultrasound Med. Biol.* **36**, 361–375 (2010).
³¹F. L. Lizzi, M. Astor, T. Liu, C. Deng, D. J. Coleman, and R. H. Silverman, "Ultrasonic spectrum analysis for tissue assays and therapy evaluation," *Int. J. Imaging Syst. Technol.* **8**, 3–10 (1997).
³²R. M. Vlad, S. Brand, A. Giles, M. C. Kolios, and G. J. Czarnota, "Quantitative ultrasound characterization of responses to radiotherapy in cancer mouse models," *Clin. Cancer Res.* **15**, 2067–2075 (2009).
³³G. J. Czarnota, M. C. Kolios, J. Abraham, M. Portnoy, F. P. Ottensmeyer, J. W. Hunt, and M. D. Sherar, "Ultrasound imaging of apoptosis: High-resolution non-invasive monitoring of programmed cell death in vitro, in situ and in vivo," *Br. J. Cancer* **81**, 520–527 (1999).
³⁴M. C. Kolios, G. J. Czarnota, M. Lee, J. W. Hunt, and M. D. Sherar, "Ultrasonic spectral parameter characterization of apoptosis," *Ultrasound Med. Biol.* **28**, 589–597 (2002).
³⁵R. H. Silverman, D. J. Coleman, F. L. Lizzi, J. H. Torpey, J. Driller, T. Iwamoto, S. E. P. Burgess, and A. Rosado, "Ultrasonic tissue characterization

- and histopathology in tumor xenografts following ultrasonically induced hyperthermia," *Ultrasound Med. Biol.* **12**, 639–645 (1986).
- ³⁶L. X. Yao, J. A. Zagzebski, and E. L. Madsen, "Backscatter coefficient measurements using a reference phantom to extract depth-dependent instrumentation factors," *Ultrason. Imaging* **12**, 57–70 (1990).
- ³⁷N. L. Bush, I. Rivens, G. R. ter Haar, and J. C. Bamber, "Acoustic properties of lesions generated with an ultrasound therapy system," *Ultrasound Med. Biol.* **19**, 789–801 (1993).
- ³⁸M. R. Gertner, B. C. Wilson, and M. D. Sherar, "Ultrasound properties of liver tissue during heating," *Ultrasound Med. Biol.* **23**, 1395–1403 (1997).
- ³⁹J. P. Kemmerer and M. L. Oelze, "Ultrasonic assessment of thermal therapy in rat liver," *Ultrasound Med. Biol.* **38**, 2130–2137 (2012).
- ⁴⁰V. Kumar, A. K. Abbas, N. Fausto, and J. C. Aster, *Pathologic Basis of Disease* (Saunders Elsevier, Philadelphia, 2010), Chap. 1, pp. 3–43.